APL Materials

RESEARCH ARTICLE | JANUARY 23 2019

On the structure, synthesis, and characterization of ultrafast blue-emitting $CsPbBr_3$ nanoplatelets

Special Collection: Perovskite Semiconductors for Next Generation Optoelectronic Applications

Kateřina Tomanová; Václav Čuba; Mikhail G. Brik; Eva Mihóková; Rosana Martinez Turtos; Paul Lecoq; Etiennette Auffray; Martin Nikl

APL Mater. 7, 011104 (2019)
https://doi.org/10.1063/1.5079300

On the structure, synthesis, and characterization of ultrafast blue-emitting $CsPbBr_3$ nanoplatelets

Cite as: APL Mater. 7, 011104 (2019); doi: 10.1063/1.5079300
Submitted: 30 October 2018 • Accepted: 4 January 2019 •
Published Online: 23 January 2019

Kateřina Tomanová,[1,a)] Václav Čuba,[1] Mikhail G. Brik,[2,3,4,5] Eva Mihóková,[5] Rosana Martinez Turtos,[6] Paul Lecoq,[6] Etiennette Auffray,[6] and Martin Nikl[5]

AFFILIATIONS

[1]Department of Nuclear Chemistry, Faculty of Nuclear Sciences and Physical Engineering, Czech Technical University in Prague, Břehová 7, Prague 115 19, Czech Republic
[2]College of Sciences, Chongqing University of Posts and Telecommunications, Chongqing 400065, People's Republic of China
[3]Institute of Physics, University of Tartu, W. Ostwald Str. 1, Tartu 50411, Estonia
[4]Institute of Physics, Jan Dlugosz University, Armii Krajowej 13/15, PL-42200 Czestochowa, Poland
[5]Department of Optical Materials, Institute of Physics of the Czech Academy of Sciences, Cukrovarnická 10, Prague 162 53, Czech Republic
[6]CERN, 1211 Geneva 23, Switzerland

Note: This paper is part of the special topic on Perovskite Semiconductors for Next Generation Optoelectronic Applications.
[a)]**Author to whom correspondence should be addressed:** Katerina.Tomanova@fjfi.cvut.cz

ABSTRACT

Recent developments in medical imaging techniques, in particular, those in time-of-flight positron emission tomography put new challenges on scintillating material performance that cannot be fulfilled by conventional scintillators. Bright and ultrafast nanoparticles represent promising candidates to build up an advanced detection system needed. We synthesize colloidal $CsPbBr_3$ nanoplatelets emitting blue light with fast sub-nanosecond decay. We also prepare a nanocomposite material by embedding the nanoplatelets in the polystyrene matrix. We show that blue emission is preserved provided the composite is not exposed to UV/vis light and/or elevated temperatures. Motivated by conflicting information from the literature about the room temperature structure of colloidal $CsPbX_3$ (X = Cl, Br, I) particles, that results being orthorhombic, rather than cubic, we perform *ab initio* electronic structure calculations of bulk crystals with an orthorhombic structure. We calculate optical properties, as well as exciton diameters and binding energies and compare them to those previously obtained for cubic $CsPbX_3$ crystals.

Inorganic scintillators are commonly used for detection of ionizing radiation in a variety of applications. A forefront field of interest focuses on medical applications, such as imaging systems for medical diagnosis.[1–5] For positron emission tomography (PET) imaging, the key performance parameters are the quality of the reconstructed image together with the possibility to detect small tumors and to access dynamically different molecular pathways with the minimum radioactive dose injected to the patient.[6] This put specific requirements on the scintillating material characteristics. In recent years, the fast timing capability received particular attention driven by the time-of-flight PET.[7–10] Desired coincidence time resolution (CTR) in the range of 100 ps FWHM can be achieved via high light yield and very short rise and decay times of the scintillation light.[11,12] In lately developed efforts to push CTR even further down to 10 ps,[13] one needs to consider mechanisms involving a production of prompt photons. One option is to create heterostructures combining standard dense scintillators like LSO and nanocrystals. The latter, due to quantum confinement, can feature enhanced optical properties, in particular, high quantum efficiency and ultrafast decay time, with respect to their bulk counterparts. Colloidal semiconductors,

such as colloidal CdSe nanosheets[14] or cesium lead halide perovskites, seem to be promising candidates to pursue.

Cesium lead halide perovskites $CsPbX_3$ (X = Cl, Br, I) are under intense investigation due to their potential applications in various fields, such as photovoltaics,[15,16] optoelectronic devices,[17–19] or X-ray and gamma-ray detectors.[20,21]

The bulk $CsPbX_3$ crystals have been reported already in 1950s.[22] Their perovskite structure undergoes phase transitions induced by temperature.[23–25] The cubic phase with the space group $Pm\bar{3}m$ is stable only at higher temperatures.[26–28] At room temperature, the bulk $CsPbCl_3$,[29] $CsPbBr_3$,[28] and $CsPbI_3$[21] possess a thermodynamically preferred orthorhombic structure with the space group Pnma.

Earlier photoluminescence studies have shown the presence of the 2.98 eV and 2.32 eV peaks in $CsPbCl_3$ and $CsPbBr_3$, respectively, that were attributed to recombination of Mott-Wannier excitons.[30–32] Formation of $CsPbX_3$ quantum dots (QDs) was observed in CsX:Pb host matrices.[33–35] Thanks to quantum confinement effect the excitonic luminescence of QDs featured subnanosecond decay times, namely, 90 ps at 10 K in $CsPbBr_3$[34] and 30 ps at 10 K in $CsPbCl_3$.[33] More recently, colloidal nanocrystal QDs of $CsPbX_3$ or mixed halide systems Cl/Br and Br/I have been synthesized.[17] Based on X-ray diffraction (XRD) patterns, the authors claimed that their structure was cubic. These QDs provide high quantum yields, narrow emission bands, and room temperature decay times within 1-29 ns. The emission is tunable within the entire visible spectral range by changing halide composition or the particle size. The latter is directly linked to quantum confinement effects that can be observed for the particle diameter comparable or smaller with respect to the delocalization length of an exciton in the corresponding bulk material. This quantity, Bohr diameter, together with exciton binding energies were calculated by density functional theory (DFT) methods and effective mass approximation for cubic structures of $CsPbX_3$.[17] However, other studies of bright colloidal $CsPbX_3$ nanocrystals bring conflicting information about their structure. Similar to the study by Protesescu *et al.*,[17] the colloidal $CsPbBr_3$ nanoplatelets[19] were also reported as cubic, while $CsPbBr_3$ QDs[36] and $CsPbX_3$ nanowires[37,38] as orthorhombic. To resolve the problem, the structure of colloidal $CsPbBr_3$ QDs was thoroughly investigated using Rietveld refinements and PDF analysis of synchrotron X-ray total scattering data.[39] Based on the results, the authors concluded that the structure was orthorhombic Pnma rather than cubic $Pm\bar{3}m$. They also pointed out that deviation in the structure may have a nontrivial impact on the electronic band structure and related quantities determined in the study by Protesescu *et al.*[17] that were based on the cubic crystal structure of the material.

Ab initio calculations of the $CsPbX_3$ electronic band structure were performed in a number of studies. Besides all halides studied by Protesescu *et al.*,[17] the cubic structure of $CsPbCl_3$ was recently also studied by Ghebouli *et al.*,[40] that of $CsPbBr_3$ in Refs. 41–43, and that of $CsPbI_3$ in Refs. 41, 42, 44, and 45. The calculations associated with the orthorhombic structure of $CsPbBr_3$ are reported in Refs. 46 and 47 and that of $CsPbI_3$ in Refs. 41, 42, 44, and 45. Nevertheless, to our knowledge, no systematic *ab initio* calculations of the electronic structure of all three cesium lead halides with orthorhombic structure Pnma have been reported. In particular, possible impact of the orthorhombic crystal structure on appearance of quantum confinement effects has not been addressed.

In this paper, we synthesize colloidal $CsPbBr_3$ nanoplatelets exhibiting strong quantum confinement effects leading to their fast subnanosecond decay. X-ray powder diffraction (XRPD) measurements of prepared material confirm its orthorhombic structure. To demonstrate the practical applicability of the material for development of the detector system, we incorporate the nanoplatelets into the polystyrene host matrix. In the light of previous conclusions[39] (confirmed as well in the present work) about the structure of $CsPbBr_3$ colloidal nanoparticles being orthorhombic, we also consider in detail the structure of $CsPbX_3$ (X = Cl, Br, I) and perform *ab initio* electronic structure calculations of $CsPbX_3$ crystals with the orthorhombic structure. In addition, we calculate physical quantities linked to quantum confinement effects that help to assess boundaries for obtaining nanoparticles with enhanced optical properties compared to the corresponding bulk material.

Following chemicals were used for preparation of $CsPbBr_3$ nanoplatelets, and $CsPbBr_3$ polystyrene nanocomposite materials: CsBr (99.999%, Sigma-Aldrich), $PbBr_2$ (99.999%, Sigma-Aldrich), N,N–dimethylformamide (DMF, anhydrous, 99.8%, Sigma-Aldrich), oleic acid (OA, 99%, Sigma-Aldrich), oleylamine (OAm, 70%, Sigma-Aldrich), toluene (anhydrous, 99.8%, Sigma-Aldrich), and polystyrene (PS, no additives, Nuvia). All chemicals were used as received without further purification.

X-ray powder diffraction (XRPD) was measured using a Rigaku Miniflex 600 diffractometer equipped with the Cu X-ray tube (average wavelength $K_{\alpha 1,2}$ 0.154 18 nm, voltage 40 kV, current 15 mA). Data were collected with a speed of 2°/min and compared with the ICDD PDF-2 database, version 2013. The transmission electron microscopy (TEM) was obtained using an EM201 microscope (Philips). The radioluminescence (RL) and photoluminescence (PL) spectra were collected using the spectrofluorimeter 5000M (Horiba Jobin Yvon) with the monochromator and photodetector TBX-04. The excitation

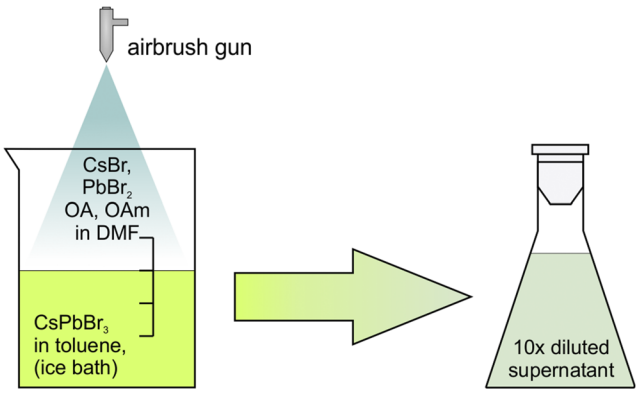

FIG. 1. Synthesis procedure of $CsPbBr_3$ using airbrush gun and ice bath.

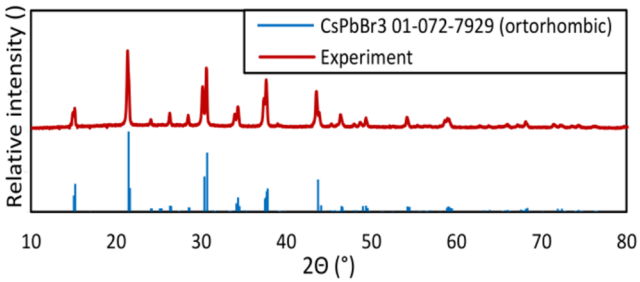

FIG. 2. XRPD pattern of the precipitated material after centrifugation.

sources were X-ray tube Seifert (40 kV, 15 mA) for radioluminescence (RL) measurements and deuterium lamp for photoluminescence (PL) measurements. The PL decays were measured using excitation by nanoLED with nanosecond pulses (300 nm). The time resolved PL spectra were obtained using the Hamamatsu C10910 streak camera with 18 ps time resolution and laser excitation (PiLAS, 372 nm).

For the synthesis, the modified procedure first described in the study by Li *et al.*[18] was used (Fig. 1).

The resulting colloidal solution exhibited a blue emission under UV excitation (365 nm). The solution was centrifuged for 10 min (12 000 g) in order to separate the largest crystals, and the supernatant was collected and characterized using XRPD (the solution was drop-casted on a glass sample holder), PL, and TEM. After characterization, the solution was diluted 10× to enhance the stability of colloidal particles (aka nanocrystals).

Embedding procedure is described in detail in the supplementary material. The resulting PS film (0.5 mm thick, 0.1 wt. % loading) also exhibited a blue emission under UV excitation (365 nm). The stability of the film evaporated at room temperature was studied at ambient conditions, and the RL spectrum was collected after 2 weeks. The second sample (see the supplementary material) was stored in the dark at 4 °C, and the RL spectrum was collected immediately after the solvent evaporation.

The XRPD pattern (Fig. 2) of the precipitated material after centrifugation (see experimental details in the supplementary

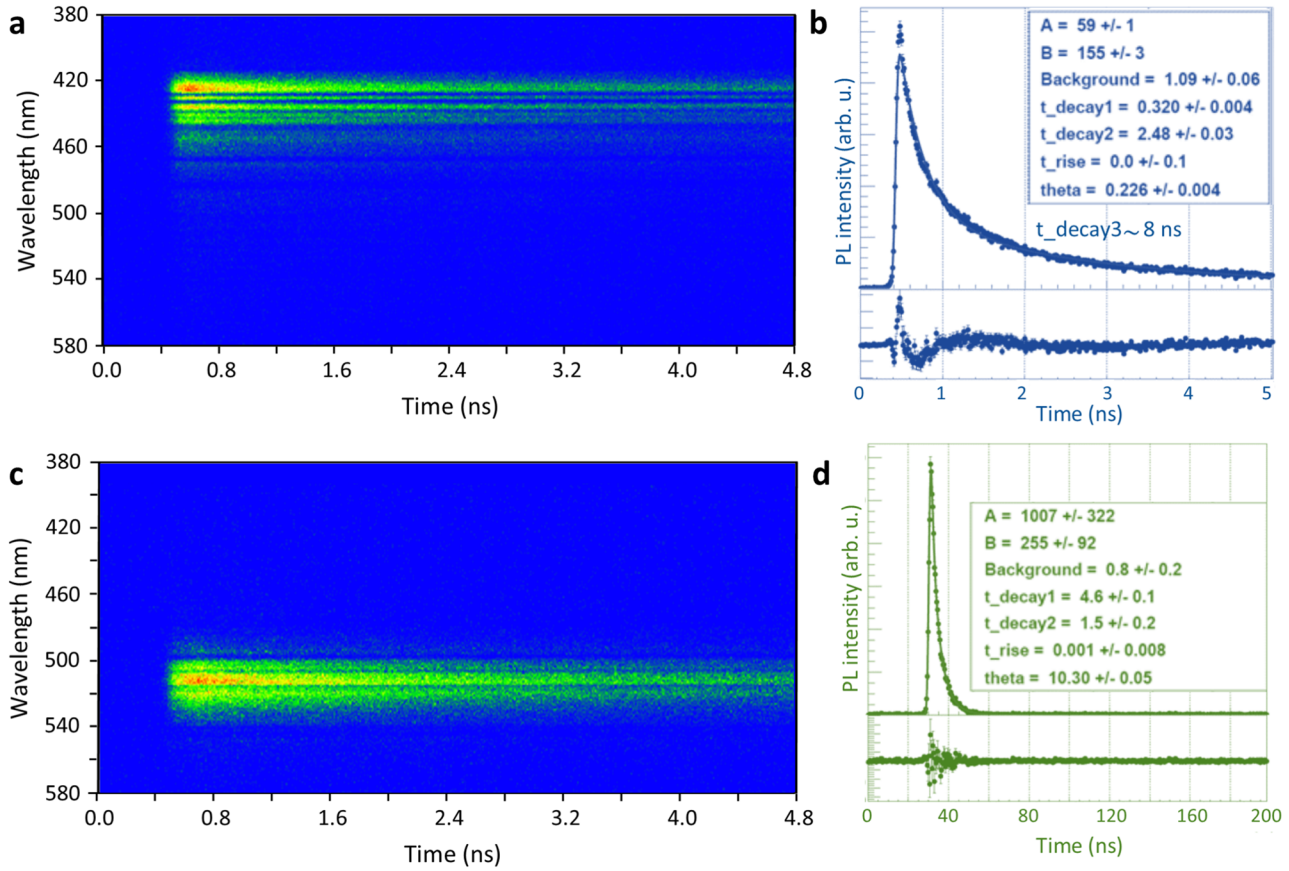

FIG. 3. Time resolved PL spectrum of the blue emission from the colloidal sample with maximum at 425 nm (a) and its decay curve (b) and time resolved PL spectrum of the green emission with maximum at 512 nm (c) and its decay curve (d). Excited by laser (372 nm).

material) compared to the ICDD PDF-2 database shows that the prepared material is orthorhombic $CsPbBr_3$.

Without slowing down the reaction rate (see experimental details in the supplementary material), the colloidal solution contained a mixture of blue and green emitting crystals. Figure 3 shows time resolved PL spectra of the colloidal sample drop-casted on a glass substrate. The results indicate the presence of two types of nanocrystals. The first type exhibits a blue emission with maximum at 425 nm, which belongs to nanocrystals with strongly quantum confined excitons. This result is further confirmed by decay measurements that show a three component decay with the fastest decay time of 320 ps [see Fig. 3(b)]. The second type of the particles exhibits green emission centered at 512 nm with slower decay longer than 1 ns.

With slowing down the reaction rate, it is possible to suppress the green emission, i.e., significantly decrease the concentration of larger nanocrystals. Figure 4(e) shows strong blue emission of the sample under the 365 nm excitation.

The size distribution of the obtained blue-emitting material is still quite broad, but the results in Fig. 4 show that the majority of the material is in the form of colloidal

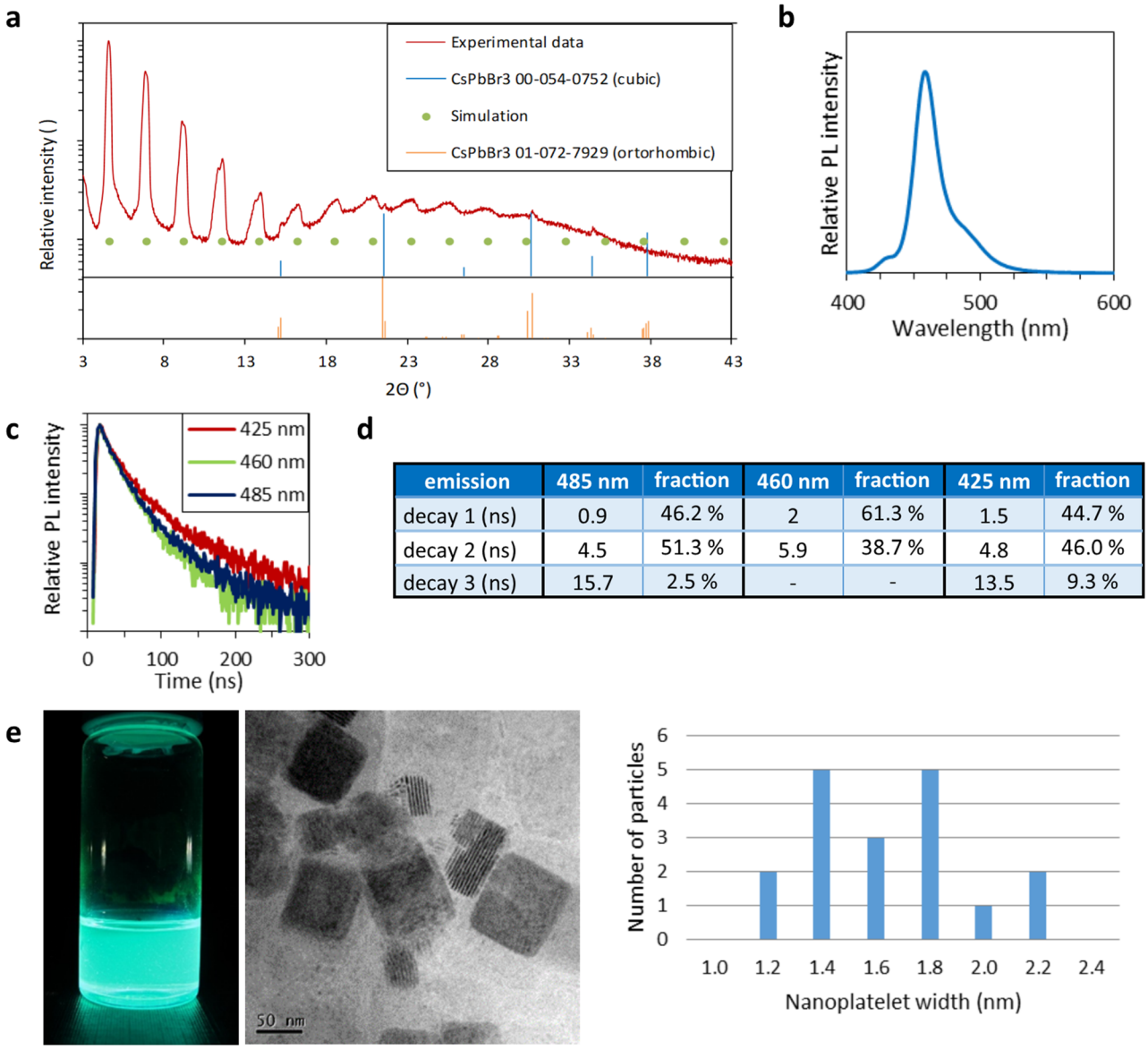

emission	485 nm	fraction	460 nm	fraction	425 nm	fraction
decay 1 (ns)	0.9	46.2 %	2	61.3 %	1.5	44.7 %
decay 2 (ns)	4.5	51.3 %	5.9	38.7 %	4.8	46.0 %
decay 3 (ns)	15.7	2.5 %	-	-	13.5	9.3 %

FIG. 4. XRPD pattern of drop-casted colloidal sample (a), PL spectrum of the colloidal sample excited by 300 nm (b), PL decay curves of all three maxima (c), and corresponding decay times (d), photograph under 365 nm excitation, TEM image, and size distribution of the nanoplatelets (e).

nanoplatelets. Another supporting evidence for this conclusion can be found in the supplementary material (absorption spectrum).

In Fig. 4(a), the XRPD pattern of a drop-casted blue-emitting film is presented. The high noise level can be explained by the presence of amorphous OA and OAm. Diffraction peaks emerging from the noise are compared to both cubic and orthorhombic phases of $CsPbBr_3$. However, high noise prevents the possibility to distinguish whether the phase is cubic or orthorhombic for the simple reason that diffraction maxima of the cubic phase are located at the same positions as the most intense diffraction maxima of the orthorhombic phase. Due to the confirmed orthorhombic phase of the precipitated material (cf. Fig. 2) and results reported in the study by Cottingham and Brutchey,[39] we believe that the present phase is orthorhombic rather than cubic. The main feature of the diffractogram is an interesting pattern of peaks with decreasing intensity. A simulation shows that it could be attributed to a repeating pattern of single lattice planes with an interplanar spacing of 38 Å. Coincidentally, based on the TEM images [Fig. 4(e)], it corresponds to the distance between two nanoplatelets stuck together.

The size distribution obtained from the TEM image in Fig. 4(e) show that based on the assumption of the orthorhombic structure (the size of the $PbBr_6$ octahedron 5.936 Å as calculated below, see Fig. 8), the majority of the nanoplatelets have a width corresponding to 2–3 monolayers.

The PL spectrum of the colloidal solution of nanoplatelets is presented in Fig. 4(b). The excitonic peak is shifted to shorter wavelengths compared to the bulk material, and its shape suggests that it is a combination of several emission bands. The emission maxima are positioned at about 430 nm, 458 nm, and 490 nm. This confirms the presence of nanoplatelets consisting of different numbers of monolayers.

The PL decay was measured for all three emission maxima; see Fig. 4(c). The fastest decay component has the decay time of 0.9 ns [Fig. 4(d)]. Compared to the result from green-emitting larger nanocrystals [1.5 ns, Fig. 3(d)], it is considerably accelerated due to strong quantum confinement effects.

Nanoplatelets of $CsPbBr_3$ were successfully embedded in a polystyrene matrix with approximately 0.1 wt. % loading. This step is crucial for a development of a detector based on this material further combined with a classical heavy scintillator with the high light yield, such as LYSO:Ce.[13] It is also necessary to enhance the overall stability of $CsPbBr_3$ nanoplatelets. Resulting composites show good optical quality and sufficient transparency; see Fig. 5.

Figure 5(a) shows a comparison of RL spectra of two samples: one stored in the dark at 4 °C and one stored at ambient conditions for 2 weeks. The emission band centered at about 320 nm belongs to a polystyrene matrix. The other band around 500 nm is attributed to $CsPbBr_3$ excitonic emission that is shifted with respect to the bulk material with the shift depending on a particle size (or more precisely the size of the largest particles present in the matrix). The 0.1 wt. % loading is apparently not enough to efficiently transfer the energy from the polystyrene matrix (320 nm emission) toward $CsPbBr_3$

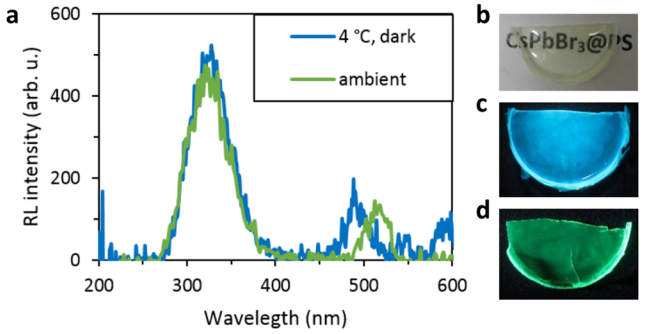

FIG. 5. RL spectrum of $CsPbBr_3$ embedded in a polystyrene stored in dark at 4 °C and of $CsPbBr_3$ embedded in a polystyrene after 2 weeks storage at ambient conditions [daylight, room temperature 30 °C (a)], photographs of samples in the daylight (b), and under 365 nm UV light [(c) for the sample kept in dark and cold, (d) for the sample kept at ambient conditions].

nanoplatelets, and further work is in progress to increase the loading at least ten times. It can be concluded that elevated temperature and the exposure to UV/vis light probably cause a diffusion of the nanoplatelets in the PS matrix. This may lead to their agglomeration into larger particles.

The local density approximation (LDA) and the general gradient approximation (GGA) methods were employed to calculate the structural, electronic, and optical properties of $CsPbX_3$ (X = Cl, Br, I). For further details on computation methods, please see the supplementary material.

All three compounds crystallize in the Pnma space group (No. 62) with four formula units in one unit cell. The Pb ions are surrounded by six halide anions, forming slightly distorted octahedra. These octahedra are corner-sharing in $CsPbCl_3$, $CsPbBr_3$ (aligned along the b axis) and are isolated from each other in $CsPbI_3$. Figures 6 and 7 show the unit cells of these materials as seen along the c and b axes.

Different characters of the PbX_6 (X = Cl, Br, I) octahedra orientation in the crystal lattices is clearly seen from these figures. Not only these octahedral units have different geometrical arrangements but their local structure also changes from one host to another. Figure 8 shows the enlarged views of the PbX_6 complexes with indication of the Pb–X distances (in Å). All halide anions in these figures are labeled by the Roman numbers to analyze the angles between the chemical bonds and assess in this way degree of deviation of each of these octahedra from the ideal octahedral symmetry.

It is easy to see then that both $PbCl_6$ and $PbBr_6$ octahedral structural units have the inversion center (the opposite chemical bonds in the octahedra are equal, and the corresponding angles are 180°), whereas the PbI_6 complex does not, as confirmed by the analysis of the interatomic distances and angles between the chemical bonds (Fig. 8 and Table S1 in the supplementary material).

The ideal octahedron has three angles of 180° (three pairs of opposite vertices) and twelve angles of 90°. It can be noticed from Table S1 (see the supplementary material) that the $PbCl_6$ complex has the highest symmetry among the

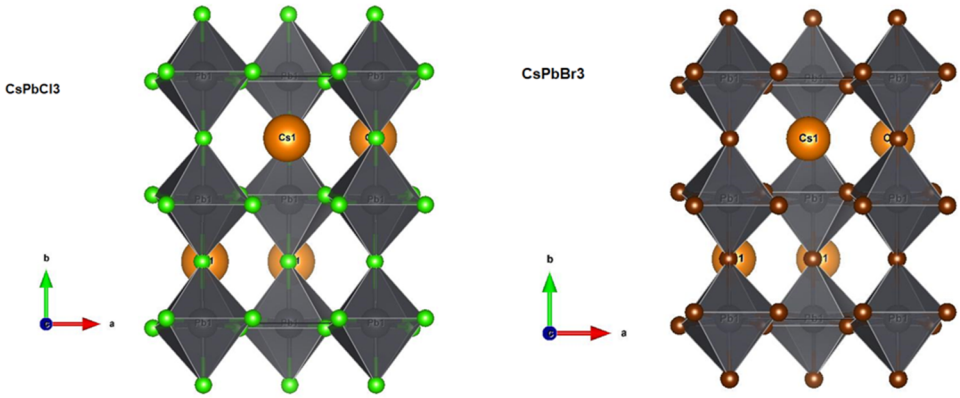

FIG. 6. One unit cell of $CsPbCl_3$, $CsPbBr_3$, and $CsPbI_3$ (a view along the *c* axis). Drawn with VESTA.[48]

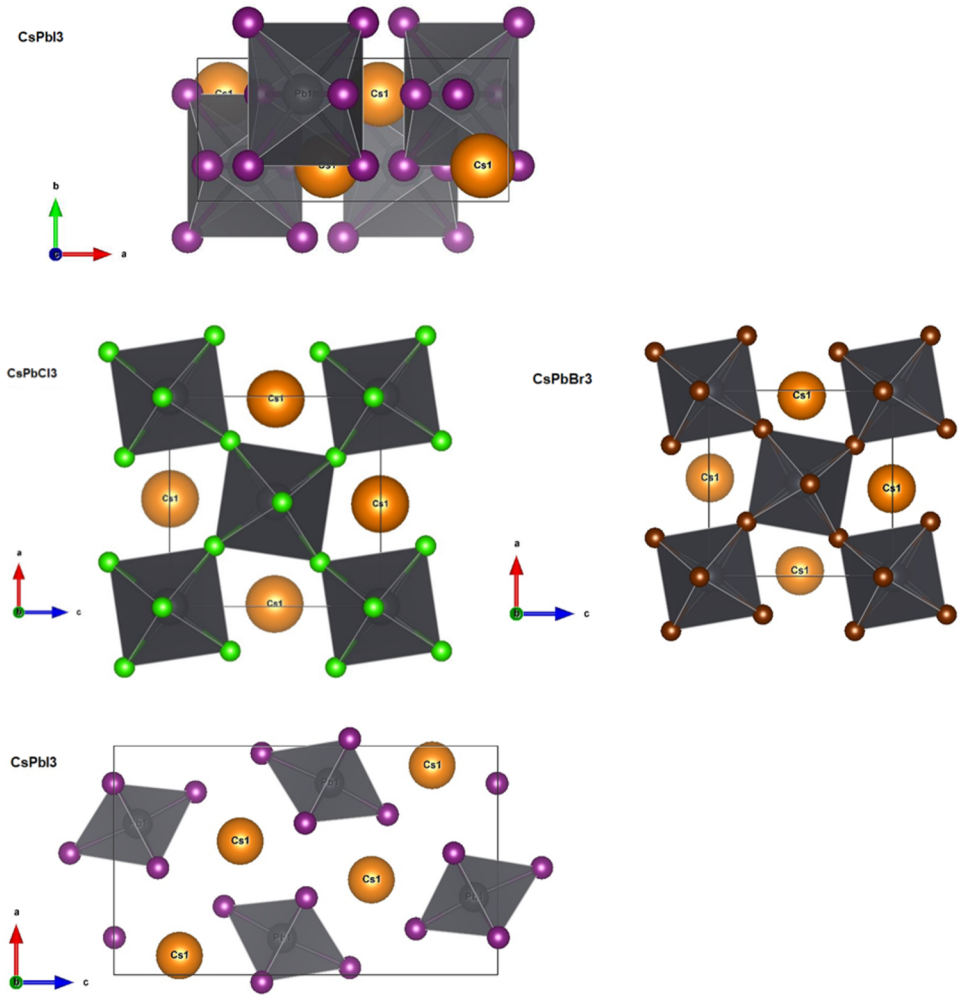

FIG. 7. One unit cell of $CsPbCl_3$, $CsPbBr_3$, and $CsPbI_3$ (a view along the *b* axis). Drawn with VESTA.[48]

considered PbX_6 units; the differences between the ideal octahedron angles and the ones in the $PbCl_6$ cluster are less than one degree. Deviations of the actual symmetry from the ideal octahedral case increase with increasing the halide ion atomic number (or its ionic radius). The PbI_6 complex loses its center of inversion and is characterized by the largest differences between its octahedral angles and an ideal octahedron among the considered three cases.

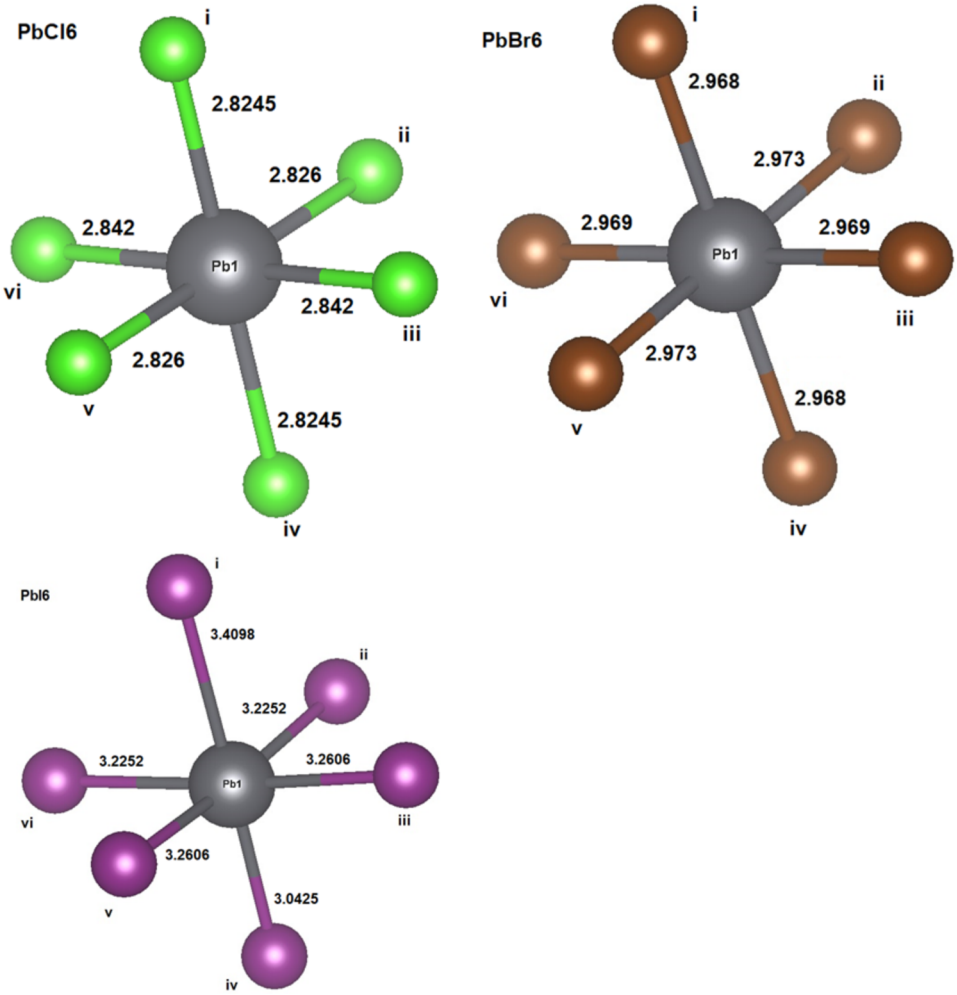

FIG. 8. Octahedral PbX_6 (X = Cl, Br, I) complexes in $CsPbCl_3$, $CsPbBr_3$, and $CsPbI_3$. The Pb-X distances (in Å) are given. Drawn with VESTA.[48]

The summary of the experimental and calculated structural data for $CsPbX_3$ is given in Table S2 in the supplementary material. Good agreement between the experimental (taken as an initial input structure) and optimized lattice constants was achieved. In addition, the calculated and experimental fractional coordinates of all ions in the unit cells agree well with each other. It can be noticed that the LDA-calculated lattice constants are always somewhat smaller than the GGA-calculated ones. Figure 9 shows the calculated band structures for all three studied crystals.

All three hosts appear to be the direct bandgap materials. The maximum of the valence band (VB) and minimum of the conduction band (CB) in $CsPbCl_3$ and $CsPbBr_3$ are realized at the G point (Brillouin zone center); however in $CsPbI_3$, such situation takes place at the Y point. It can be, however, noted that in the case of the chloride and bromide materials, the CB minima at the G and X points are practically equal, which may imply certain ambiguity in determination of the bandgap character, both theoretically and experimentally. There is a remarkable difference in the character of the calculated bands between $CsPbCl_3$ and $CsPbBr_3$ on the one hand and $CsPbI_3$ on the other hand. If for the former two compounds the VB and CB states exhibit pronounced dispersion and there are rather deep valleys away from the G point, for the latter material, the electronic states at the VB top are practically flat, which indicates very low mobility of the holes in $CsPbI_3$. This may be due to the isolated PbI_6 units in the compound. Similarly, flat profiles of the VB top states were obtained in earlier publications.[41,42,44] The CB states in $CsPbI_3$ are also rather flat, except for the Y–S direction, showing a low mobility of the electrons as well.

The origin of the electronic states in the calculated bands can be understood with the help of the density of states (DOS) diagrams, as shown in Fig. 10.

The lower CB states in all studied halides are composed of the lead 6p orbitals; the upper CB states are made up by the Cs 6s states. The central parts of the VB are dominating by the halides p states (3p for Cl, 4p for Br, and 5p for I), but an important feature is that the topmost VB levels are due to the Pb 6s states, so the lower energy part of

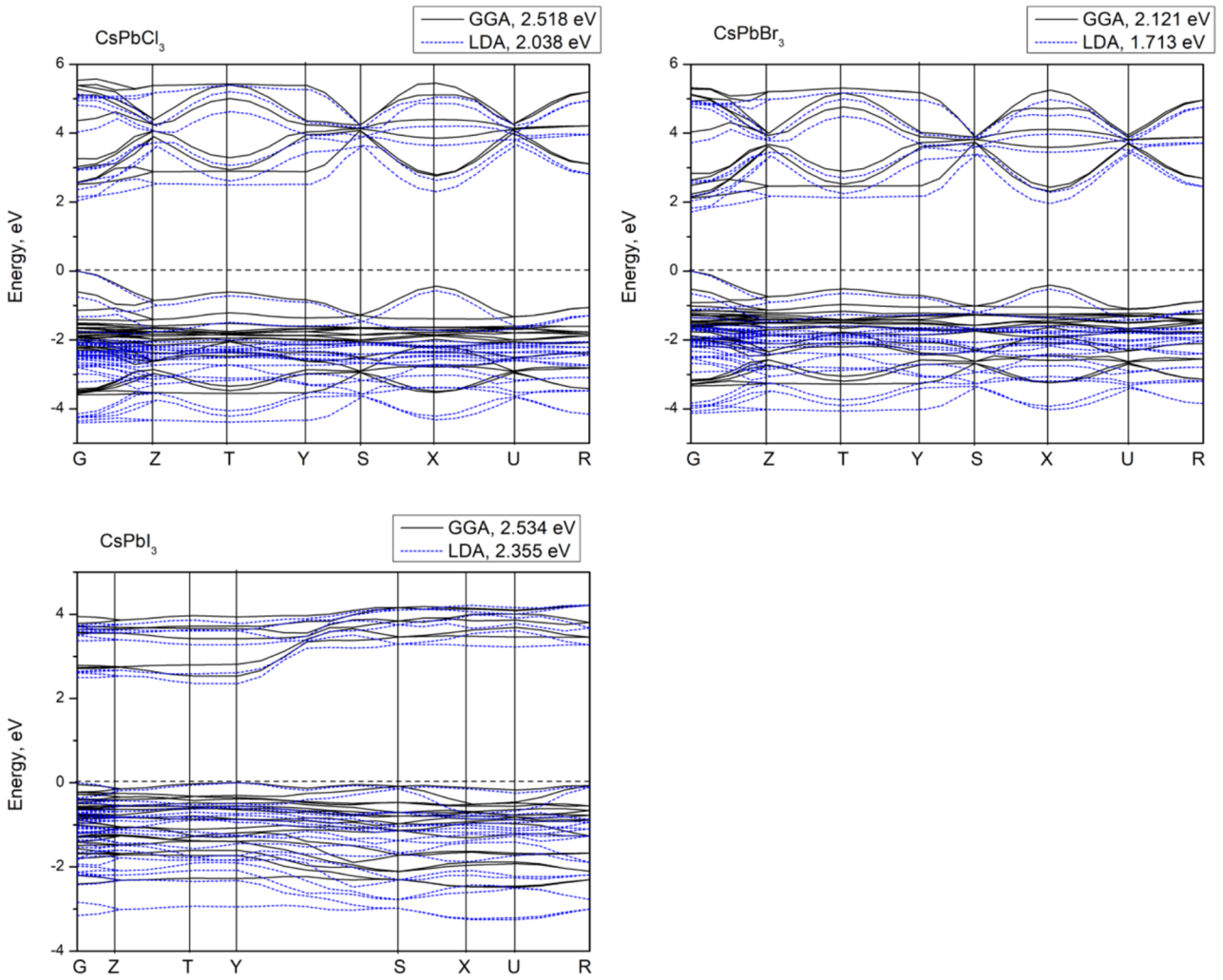

FIG. 9. Calculated band structures of $CsPbCl_3$, $CsPbBr_3$, and $CsPbI_3$. The GGA- and LDA-calculated results are shown by the solid and dashed lines, respectively. The calculated bandgaps are given at the top of each diagram. The coordinates of the special points of the Brillouin zone are (in the units of the reciprocal lattice unit vectors) G(0, 0, 0); Z(0, 0, ½); T(−½, 0, ½), Y(−½, 0, 0); S(−½, ½, 0); and X(0, ½, 0), U(0, ½, ½), R(−½, ½, ½).

the band-to-band absorption can be associated with the 6s–6p Pb excitation. It can also be noticed that the VB in $CsPbI_3$ is somewhat narrower than in two other halides. The overall pattern of the Cs and Pb states in all three crystals is practically the same. The Cs 5s states appear as a sharp maximum at around −21 eV, and the Cs 5p states produce the lower VB at about −7.5 eV. The lead 5d states are located at about −16 eV. The 3s, 4s, and 5s states of the Cl, Br, and I ions, respectively, move slightly closer to the upper VB bottom. The DOS diagrams and bands assignment for $CsPbCl_3$ and $CsPbBr_3$ agree well with the data from Ref. 49. It should be emphasized that most of the first-principles calculations for the title compounds were made for their cubic phase, e.g., Refs. 17, 40, and 43 and, therefore, cannot be compared directly with the current results. A few data available on the experimental and calculated band structures of orthorhombic $CsPbI_3$ are collected in Table I.

The calculated unpolarized dielectric functions for $CsPbCl_3$, $CsPbBr_3$, and $CsPbI_3$ are shown in Fig. 11 (see the supplementary material for details on how to calculate them). The values of $\mathrm{Re}(\varepsilon)$ in the limit of infinite wavelength determine the refractive index of a solid $n = \sqrt{\mathrm{Re}(\varepsilon)}$. Since the studied crystals are all orthorhombic, they should be optically anisotropic, as is evidenced by the data in Table S3 that collects the calculated in the present work $\mathrm{Re}(\varepsilon)$ values along the crystallographic axis with other data available in the literature.

For the relevant equations for the estimation of the effective masses of electrons and holes (m_h^*, m_e^*), the exciton

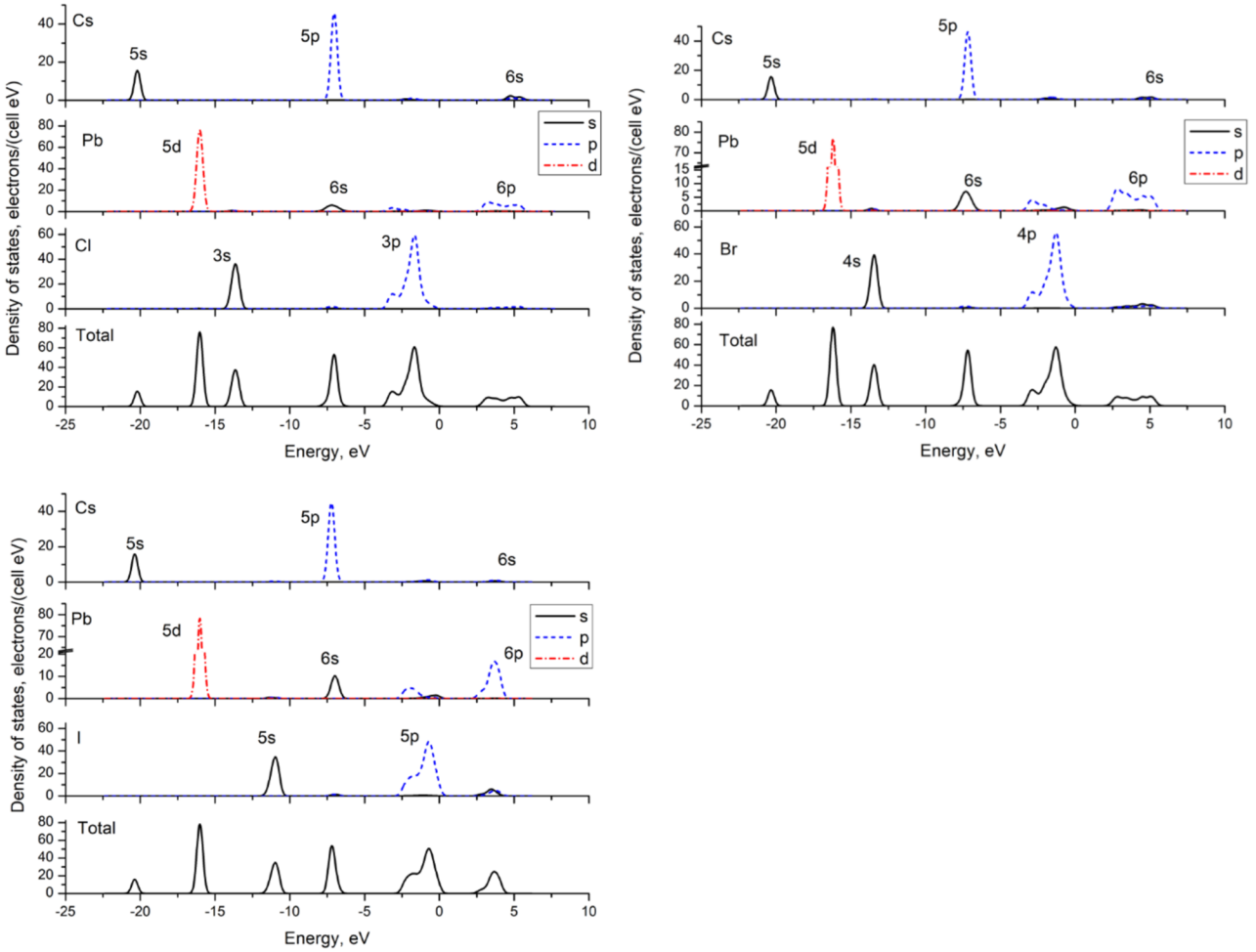

FIG. 10. Calculated density of states (DOS) diagrams for $CsPbCl_3$, $CsPbBr_3$, and $CsPbI_3$.

diameter a_0 and the exciton binding energy E_b see the supplementary material.

The results of estimations of all these parameters for the studied halides are collected in Table II. Some indirect comparison can be made with the data obtained in Ref. 17, but it should be kept in mind that those results were obtained for the cubic modifications of these halides. The band structures calculated in that reference are very similar to each other and exhibit strong dispersion around the VB maxima and CB minima. This is not the case for the orthorhombic phases, especially for $CsPbI_3$, where the VB top is remarkably flat, which leads to very high values of the hole effective mass.

TABLE I. Calculated and experimental bandgaps for $CsPbI_3$.

	Expt.	Calculated		
Bandgap (eV)	3.17	2.534, 2.355	2.54	2.29
References	50	This work	45	28

A large difference between the effective masses of the electrons and holes in $CsPbI_3$ can be attributed to very contrast behavior of the electronic states at the VB top and the CB bottom (Fig. 9): it is easy to see that the curvatures of those states are quite different and so are the corresponding effective masses.

Synthesized colloidal nanocrystals of $CsPbBr_3$ were characterized by XRPD, steady state, and time resolved PL and TEM. XRPD confirms their orthorhombic structure. Under UV excitation, the nanocrystals exhibit ultrafast blue subnanosecond emission due to strong quantum confinement effects or green emission (somewhat longer than a nanosecond) depending on the particle size. The green emission of larger nanocrystals can be suppressed by slowing down the reaction and agglomeration rate. Drop-casted blue emitting film shows the presence of nanoplatelets with a width of 2-3 monolayers. Its PL spectrum composed of several bands confirms the presence of nanoplatelets consisting of different numbers of monolayers. The fastest PL decay is below

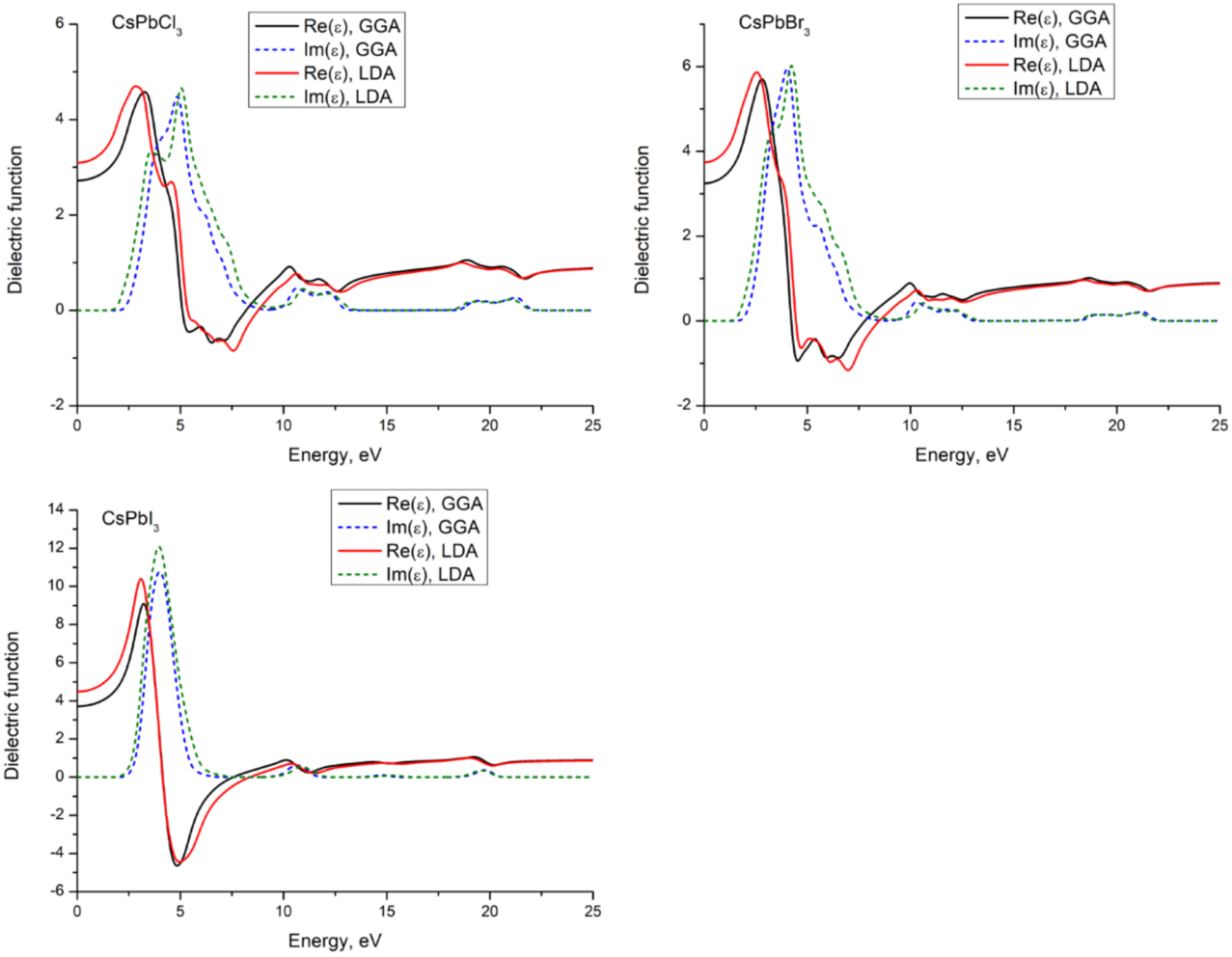

FIG. 11. Calculated dielectric function for $CsPbCl_3$, $CsPbBr_3$, and $CsPbI_3$.

1 ns. To test the applicability of prepared nanoplatelets, they were embedded in the polystyrene matrix. The subnanosecond blue emission in this nanocomposite can be preserved provided the sample is not exposed to the UV/vis light and/or high temperatures. Such emission makes the $CsPbBr_3$ nanocomposite material further combined with a classical

TABLE II. Calculated effective masses of the holes and electrons (in the units of the electron mass) and Wannier-Mott exciton parameters for $CsPbCl_3$, $CsPbBr_3$, and $CsPbI_3$.

	$CsPbCl_3$			$CsPbBr_3$			$CsPbI_3$		
	GGA	LDA	Calc.[a]	GGA	LDA	Calc.[a]	GGA	LDA	Calc.[a]
m_h^*	0.10	0.09	0.17	0.12	0.10	0.14	1.4	1.1	0.13
m_e^*	0.23	0.19	0.20	0.26	0.23	0.15	0.08[b]	0.08[b]	0.11
ε_∞[c]	2.723	3.09	4.07	3.247	3.74	4.96	3.72	4.49	6.32
a_0 (Å)	41	55	50	42	55	70	48	58	120
E_b (meV)	130	85	75	106	70	40	80	55	12

[a]Reference 17, for the cubic phase.
[b]Estimations of the m_e^* were performed for the Y–S path (Fig. 9), where dispersion of the electronic states is the strongest.
[c]ε_∞ denotes the dielectric constant value in the limit of infinite wavelengths.

heavy scintillator with the high light yield, such as LYSO:Ce, a promising candidate for building up the time-of-flight positron emission tomography (TOF-PET) detector.

Detailed consideration of the structural properties of $CsPbX_3$ halides (X = Cl, Br, I) revealed an important difference among these materials: the $PbCl_6$ and $PbBr_6$ octahedra are connected by vertices, whereas the PbI_6 octahedra are isolated from each other. In addition, the local symmetry of the halide octahedra around the Pb ions decreases with increased halide atomic number. The optimized unit cells and all their structural characteristics agreed well with the experimental XRD data. The calculated band structures show all compounds to be direct bandgap materials although an indirect bandgap transitions at the same energy can be realized in $CsPbCl_3$ and $CsPbBr_3$ since the conduction bands minima at two different points of the Brillouin zone are practically equal in these compounds. The effective masses of the electrons for the lowest states in the conduction band and holes for the highest states in the valence bands were performed. It was shown that the effective masses of holes in $CsPbI_3$ are very large because the top of the valence band in this halide is nearly flat. We believe that the isolated character of the PbI_6 octahedra may be behind a low hole's mobility in $CsPbI_3$.

In addition to the calculations of the structural, electronic, and optical properties of these three halide materials, we estimated the effective exciton diameter and exciton binding energy. The exciton diameter increases and the binding energy decreases with increasing halide atomic number.

See supplementary material for details on synthesis, absorption spectrum of colloidal nanoplatelets, computational methods, and additional data on structural calculations.

This work was carried out in the frame of Crystal Clear Collaboration and has been supported by the Czech Science Foundation, Grant No. GA17-06479S, the Ministry of Education Youth and Sports, project "Center for advanced applied science," No. CZ.02.1.01/0.0/0.0/16_019/0000778, Cost Action TD1401, ERC advanced Grant TICAL (No. 338953), and H2020 Twinning project ASCIMAT (No. 690599). M.G.B. thanks the financial support from the project MOBILITY FZU from Operational Programme: Research, Development and Education, MEYS, No. CZ.02.2.69/0.0/0.0/16_027/0008215, Recruitment Program of High-end Foreign Experts (Grant No. GDW20145200225), the Programme for the Foreign Experts offered by Chongqing University of Posts and Telecommunications, Estonian Research Council Grant PUT PRG111, and European Regional Development Fund (No. TK141). Dr. G. A. Kumar (University of Texas at San Antonio) is thanked for allowing use Materials Studio. Dr. A. Khan and Professor Dr. I. Moreels are thanked for advising us on the embedding procedure in the polystyrene.

REFERENCES

[1] R. Hofstadter, Phys. Rev. **75**, 796 (1949).
[2] C. W. E. Van Eijk, Phys. Med. Biol. **47**, R85 (2002).
[3] C. W. E. Van Eijk, Nucl. Instrum. Methods Phys. Res., Sect. A **509**, 17 (2003).
[4] P. Lecoq, Nucl. Instrum. Methods Phys. Res., Sect. A **809**, 130 (2016).
[5] C. Ronda, H. Wieczorek, V. Khanin, and P. Rodnyi, ECS J. Solid State Sci. Technol. **5**, R3121 (2016).
[6] M. Salomoni, R. Potts, E. Auffray, and P. Lecoq, Crystals **8**, 78 (2018).
[7] J. S. Karp, S. Surti, M. E. Daube-Witherspoon, and G. Muehllehner, J. Nucl. Med. **49**, 462 (2008).
[8] T. Jones and D. Townsend, J. Med. Imaging **4**, 011013 (2017).
[9] S. Gundacker, F. Acerbi, E. Auffray, A. Ferri, A. Gola, M. V. Nemallapudi, G. Paternoster, C. Piemonte, and P. Lecoq, J. Instrum. **11**, P08008 (2016).
[10] N. Aubry, E. Auffray, F. B. Mimoun, N. Brillouet, R. Bugalho, E. Charbon, O. Charles, D. Cortinovis, P. Courday, and A. J. Cserkaszky, J. Instrum. **8**, C04002 (2013).
[11] S. Gundacker, "Time resolution in scintillator based detectors for positron emission tomography," Ph.D. thesis, Vienna University of Technology, Wien, Austria, 2014.
[12] P. Lecoq, E. Auffray, S. Brunner, H. Hillemanns, P. Jarron, A. Knapitsch, T. Meyer, and F. Powolny, IEEE Trans. Nucl. Sci. **57**, 2411 (2010).
[13] P. Lecoq, IEEE Trans. Radiat. Plasma Med. Sci. **1**, 473 (2017).
[14] J. Q. Grim, S. Christodoulou, F. Di Stasio, R. Krahne, R. Cingolani, L. Manna, and I. Moreels, Nat. Nanotechnol. **9**, 891 (2014).
[15] M. M. Lee, J. Teuscher, T. Miyasaka, T. N. Murakami, and H. J. Snaith, Science **338**, 643 (2012).
[16] H.-S. Kim, C.-R. Lee, J.-H. Im, K.-B. Lee, T. Moehl, A. Marchioro, S.-J. Moon, R. Humphry-Baker, J.-H. Yum, J. E. Moser, M. Grätzel, and N.-G. Park, Sci. Rep. **2**, 591 (2012).
[17] L. Protesescu, S. Yakunin, M. I. Bodnarchuk, F. Krieg, R. Caputo, C. H. Hendon, R. X. Yang, A. Walsh, and M. V. Kovalenko, Nano Lett. **15**, 3692 (2015).
[18] X. Li, Y. Wu, S. Zhang, B. Cai, Y. Gu, J. Song, and H. Zeng, Adv. Funct. Mater. **26**, 2435 (2016).
[19] Y. Bekenstein, B. A. Koscher, S. W. Eaton, P. Yang, and A. P. Alivisatos, J. Am. Chem. Soc. **137**, 16008 (2015).
[20] Z. Liu, J. A. Peters, C. C. Stoumpos, M. Sebastian, B. W. Wessels, J. Im, A. J. Freeman, and M. G. Kanatzidis, Proc. SPIE **8852**, 88520A (2013).
[21] C. C. Stoumpos, C. D. Malliakas, J. A. Peters, Z. Liu, M. Sebastian, J. Im, T. C. Chasapis, A. C. Wibowo, D. Y. Chung, A. J. Freeman, B. W. Wessels, and M. G. Kanatzidis, Cryst. Growth Des. **13**, 2722 (2013).
[22] C. K. Møller, Nature **182**, 1436 (1958).
[23] M. Natarajan and B. Prakash, Phys. Status Solidi A **4**, K167 (1971).
[24] S. Hirotsu, J. Harada, M. Iizumi, and K. Gesi, J. Phys. Soc. Jpn. **37**, 1393 (1974).
[25] J. Hutton, R. J. Nelmes, G. M. Meyer, and V. R. Eiriksson, J. Phys. C: Solid State Phys. **12**, 5393 (1979).
[26] S. Sharma, N. Weiden, and A. Weiss, Z. Phys. Chem. **175**, 63 (1992).
[27] D. M. Trots and S. V. Myagkota, J. Phys. Chem. Solids **69**, 2520 (2008).
[28] C. C. Stoumpos, C. D. Malliakas, and M. D. Kanatzidis, Inorg. Chem. **52**, 9019 (2013).
[29] S. Plesko, R. Kind, and J. Roos, J. Phys. Soc. Jpn. **45**, 553 (1978).
[30] I. P. Pashuk, N. S. Pidzyrailo, and M. G. Matsko, Fiz. Tverd. Tela **23**, 2162 (1981).
[31] K. Nitsch, V. Hamplová, M. Nikl, K. Polák, and M. Rodová, Chem. Phys. Lett. **258**, 518 (1996).
[32] D. Fröhlich, K. Heidrich, H. Künzel, G. Trendel, and J. Treusch, J. Lumin. **18-19**, 385 (1979).
[33] M. Nikl, K. Nitsch, K. Polak, G. P. Pazzi, P. Fabeni, D. S. Citrin, and M. Gurioli, Phys. Rev. B **51**, 5192 (1995).
[34] M. Nikl, K. Nitsch, E. Mihóková, K. Polák, P. Fabeni, G. P. Pazzi, and M. Gurioli, Physica E **4**, 323 (1999).
[35] V. Babin, P. Fabeni, M. Nikl, K. Nitsch, G. P. Pazzi, and S. Zazubovich, Phys. Status Solidi B **226**, 419 (2001).
[36] A. Swarnkar, R. Chulliyil, V. K. Ravi, M. Irfanullah, A. Chowdhury, and A. Nag, Angew. Chem., Int. Ed. **127**, 15644 (2015).
[37] D. Zhang, S. W. Eaton, Y. Yu, L. Dou, and P. Yang, J. Am. Chem. Soc. **137**, 9230 (2015).

[38]D. Zhang, Y. Yang, Y. Bekenstein, Y. Yu, N. A. Gibson, A. B. Wong, S. W. Eaton, N. Kornienko, Q. Kong, M. Lai, A. P. Alivisatos, S. R. Leone, and P. Yang, J. Am. Chem. Soc. **138**, 7236 (2016).
[39]P. Cottingham and R. L. Brutchey, Chem. Commun. **52**, 5246 (2016).
[40]M. A. Ghebouli, B. Ghebouli, and M. Fatmi, Physica B **406**, 1837 (2011).
[41]J. Brgoch, A. J. Lehner, M. Chabinyc, and R. Seshadri, J. Phys. Chem. C **118**, 27721 (2014).
[42]J. Even, L. Pedesseau, J.-M. Jancu, and C. Katan, J. Phys. Chem. Lett. **4**, 2999 (2013).
[43]G. Moschou, A. Koliogiorgos, and I. Galanakis, Phys. Status Solidi A **215**, 1700941 (2018).
[44]S. X. Tao, X. Cao, and P. A. Bobbert, Sci. Rep. **7**, 14386 (2017).
[45]Y. Huang, W.-J. Yin, and Y. He, J. Phys. Chem. C **122**, 1345 (2018).
[46]J. Kang and L.-W. Wang, J. Phys. Chem. Lett. **8**, 489 (2017).
[47]M. Sebastian, J. A. Peters, C. C. Stoumpos, J. Im, S. S. Kostina, Z. Liu, M. G. Kanatzidis, A. J. Freeman, and B. W. Wessels, Phys. Rev. B **92**, 235210 (2015).
[48]K. Momma and F. Izumi, J. Appl. Crystallogr. **44**, 1272 (2011).
[49]K. Heidrich, W. Schäfer, M. Schreiber, J. Söchtig, G. Trendel, J. Treusch, T. Grandke, and H. J. Stolz, Phys. Rev. B **24**, 5642 (1981).
[50]O. N. Yunakova, V. K. Miloslavskii, and E. N. Kovalenko, Opt. Spectrosc. **112**, 91 (2012).